Physiological Measurement

IPEM
Institute of Physics and Engineering in Medicine

PAPER • OPEN ACCESS

Calibration of a three-state cell death model for cardiomyocytes and its application in radiofrequency ablation

To cite this article: Argyrios Petras *et al* 2023 *Physiol. Meas.* **44** 065003

IOP Publishing Physiol. Meas. 44 (2023) 065003 https://doi.org/10.1088/1361-6579/acdcdd

Physiological Measurement

IPEM Institute of Physics and Engineering in Medicine

OPEN ACCESS

RECEIVED
23 February 2023

REVISED
18 May 2023

ACCEPTED FOR PUBLICATION
8 June 2023

PUBLISHED
27 June 2023

PAPER

Calibration of a three-state cell death model for cardiomyocytes and its application in radiofrequency ablation

Argyrios Petras[1], **Massimiliano Leoni**[1], **Jose M Guerra**[2] **and Luca Gerardo-Giorda**[1,3]

[1] Johann Radon Institute for Computational and Applied Mathematics (RICAM), Austrian Academy of Sciences, Linz, Austria
[2] Department of Cardiology, Hospital de la Santa Creu i Sant Pau, IIB SANT PAU, Universitat Autónoma de Barcelona, CIBER CV, Barcelona, Spain
[3] Institute for Mathematical Methods in Medicine and Data-Based Modelling, Johannes Kepler University, Altenbergerstrasse 69, A-4040 Linz, Upper Austria, Austria

E-mail: luca.gerardo-giorda@jku.at

Keywords: thermal damage, cardiomyocytes, radiofrequency ablation, computer simulation

Abstract

Objective. Thermal cellular injury follows complex dynamics and subcellular processes can heal the inflicted damage if insufficient heat is administered during the procedure. This work aims to the identification of irreversible cardiac tissue damage for predicting the success of thermal treatments. *Approach.* Several approaches exist in the literature, but they are unable to capture the healing process and the variable energy absorption rate that several cells display. Moreover, none of the existing models is calibrated for cardiomyocytes. We consider a three-state cell death model capable of capturing the reversible damage of a cell, we modify it to include a variable energy absorption rate and we calibrate it for cardiac myocytes. *Main results.* We show how the thermal damage predicted by the model response is in accordance with available data in the literature on myocytes for different temperature distributions. When coupled with a computational model of radiofrequency catheter ablation, the model predicts lesions in agreement with experimental measurements. We also present additional experiments (repeated ablations and catheter movement) to further illustrate the potential of the model. *Significance.* We calibrated a three-state cell death model to provide physiological results for cardiac myocytes. The model can be coupled with ablation models and reliably predict lesion sizes comparable to experimental measurements. Such approach is robust for repeated ablations and dynamic catheter-cardiac wall interaction, and allows for tissue remodelling in the predicted damaged area, leading to more accurate in-silico predictions of ablation outcomes.

1. Introduction

Thermal treatments are common procedures performed on patients with cardiac arrhythmias. For severe cases, thermal energy is typically delivered to the target arrhythmogenic tissue via radiofrequency (Huang and Wood 2014), inducing thermal damage. At a cellular level, prolonged exposure to high temperatures results in protein denaturation and irreversible damage (Pearce 2013, Liu *et al* 2018). Moreover, a delayed cellular death has also been observed for cells that suffered injuries beyond recovery, through intrinsic mechanisms such as, among others, apoptosis or necroptosis (O'Neill *et al* 2011, Pearce 2013).

While Penne's Bioheat equation is the standard to describe the power delivery to the tissue in computational models of radiofrequency ablation (RFA, see, e.g. Singh and Melnik 2020), several models have been introduced to assess the irreversible cellular damage and estimate the resulting lesion size. As irreversible damage is expected for temperatures above 50 °C (Haines 2011), the simplest approach is the use of the 50 °C isotherm contour to identify the lesion boundary (Petras *et al* 2019, Ahn and Kim 2021, Gómez-Barea *et al* 2022, Gu *et al* 2022). This approach is typically overestimating the myocardial lesion size (Haines 2011, Liu *et al* 2018) and does not allow a physiologically accurate assessment of the lesion, particularly in the case of dynamic catheter-tissue interactions. Another approach uses a two-state Arrhenius model (Pearce 2013, Qin *et al* 2014) to model the transition of the

cells from native to denaturated state. Despite being widely used, in particular in RFA (González-Suárez *et al* 2022), it is well known that this model greatly overpredicts the shoulder region at low temperatures, where the dynamics of the thermal damage are slower (O'Neill *et al* 2011, Pearce 2013, Liu *et al* 2018). This shortcoming is particularly relevant for thermal damage of myocytes, since it is known that at 48 °C the damage is reversible for all treatment times (Zaltieri *et al* 2021), while irreversible damage is expected between 50°C and 56 °C for up to 60 s of ablation (Haines 2011). The recovery of the tissue damage, correlated to the heat shock proteins HSP70 expression, among other intrinsic protective mechanisms (Rylander *et al* 2005), cannot be captured by the two-state Arrhenius model, thus leading inevitably to inaccurate injury assessment. In this direction, the three-state thermal cell damage model initially presented in Park *et al* (2016) is capable of capturing the reversible damage of a cell, which makes it appealing for lesion estimation in radiofrequency catheter ablation models (Qadri *et al* 2017, Singh and Melnik 2019, Molinari *et al* 2022a, 2022b), although the model itself is not specific to myocytes. As a matter of fact, not only was the three-state model calibrated to bovine chordae tendineae tissue, but also all the existing two-state Arrhenius models were calibrated for a variety of different cells (Hep G2 human liver hepatocellular carcinoma and MRC-5 human lung fibroblast (O'Neill *et al* 2011), AT-1 prostate cancer cells, HDF human dermal fibroblasts, LNCaP prostate tumor cell and HuH-7 liver cancer cell (Qin *et al* 2014) and CHO Chinese hamster ovary cells, among others (Pearce 2013)), none of which were myocytes: hence the direct application of these models in the assessment of lesion formation is, at best, not advisable. Moreover, many cell types exhibit higher energy absorption when exposed to low temperatures and lower energy absorption when exposed to higher temperatures (Dewey *et al* 1977, Pearce 2013). None of the existing Arrhenius-type models of the three-state from Park *et al* (2016) is taking this aspect into account, as they all consider a unique absorption rate instead.

In this work, in order to surpass all the above limitations, we consider a modification of the three-state model from Park *et al* (2016) that accounts for the variable energy absorption rate and is calibrated for myocytes. In particular, we modify the transition phases using a piecewise linear Arrhenius model, that changes slope at 55 °C, a decision supported by experimental evidence (Dewey *et al* 1977, Pearce 2013). The calibration of the model for cardiac myocytes is then twofold. On the one hand, the model returns a response of the cardiac tissue to thermal exposure in line with available experimental data (Haines 2011, Zaltieri *et al* 2021). On the other hand, when coupled with our previously validated computational model (Petras *et al* 2019), the model reproduces lesion sizes comparable to the *in vitro* experiments in Petras *et al* (2019) for standard ablation protocols and the reported lesions in Kotadia *et al* (2019) for High Power Short Duration (HPSD) protocols. As an illustration of its capabilities, the calibrated model is then applied to assess the thermal damage in the case of repeated HPSD ablations and in the case of the wall-induced movement of the catheter during the cardiac cycle.

2. Materials and methods

We consider here the three-state thermal cell death model initially proposed in Park *et al* (2016) as a starting point. The model consists of three cellular states: the native (N) state, representing a normally functional cell, the unfolded (U) state for cells that suffered some damage that might be reversible, and the denaturated (D) state, where the cell is irreversibly damaged. The interaction of the three states can be summarized as

$$N \underset{k_3(T)}{\overset{k_1(T)}{\rightleftharpoons}} U \xrightarrow{k_2(T)} D, \tag{1}$$

where $k_i(T)$, $i = 1, 2, 3$ are temperature-dependent transition rates among the different states, T denoting the temperature. The interactions in (1) are governed by the system of ordinary differential equations

$$\begin{aligned} \frac{dN}{dt} &= -k_1(T)N + k_3(T)U, \\ \frac{dU}{dt} &= k_1(T)N - (k_2(T) + k_3(T))U, \\ \frac{dD}{dt} &= k_2(T)U. \end{aligned} \tag{2}$$

The system is initialised by considering all cells to be in native state, i.e. $N = 1$, $U = 0$ and $D = 0$. Due to the limited cardiomyocyte proliferation in mammalian hearts (He and Zhou 2017), no cell proliferation is considered in the model and a conservation equation holds at all times for the three states ($N + U + D = 1$).

In the original formulation of Park *et al* (2016), the transitions among the phases are modelled using an Arrhenius type model $k_i(T) = A_i e^{-\Delta E_i/(RT)}$, $i = 1, 2, 3$, where A_i is the frequency factor (in s^{-1}), ΔE_i is the activation energy (in $Jmol^{-1}$) and R is the universal gas constant. However, this approach does not account for the difference in energy absorption observed following a temperature increase (Qin *et al* 2014). In particular, a change in the rate of energy absorption of cells has been reported, typically occurring at around 43 °C

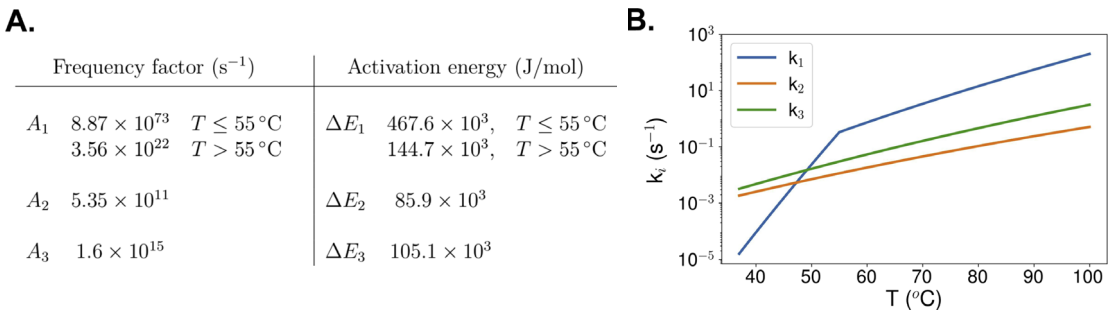

Figure 1. (A) Calibrated parameters of the three-state model. (B) Transition rates $k_i(T)$ as a function of the temperature.

(Dewey *et al* 1977, Pearce 2013). Several studies have considered a piecewise linear energy absorption rate for thermal damage, with higher energy absorption rates for temperatures below some given thresholds, which vary from 43 °C to 53 °C (Pearce 2013). Other data reports much higher absorption rates at 50 °C than at 70 °C, which appear consistent with experiments using different cell types (Qin *et al* 2014). In particular, figure 7(b) from Qin *et al* (2014) shows a large decrease in the absorption rates between 50 °C and 60 °C and a smaller one as the temperature increases further to 70 °C.

Following this experimental evidence, we consider a discontinuity in the energy absorption parameters of the transition k_1 between the native and the unfolded states at 55 °C. The model parameters are calibrated as described in section 3.1, and summarized in figure 1 panel A. As shown in panel B of the same figure, the resulting transition rate k_1 between the N and U states is continuous across $T = 55$ °C, and exhibits a slope change at $T = 55$ °C, reflecting the regime change in absorption rates.

Following Park *et al* (2016), the overall frequency factor and activation energy are given as $A = A_1A_2/A_3$ and $\Delta E = \Delta E_1 + \Delta E_2 - \Delta E_3$ respectively. For $T \leqslant 55$ °C we obtain $A = 2.97 \times 10^{70}\ s^{-1}$ and $\Delta E = 448.4 \times 10^3\ J\ mol^{-1}$, which is consistent with the experimental data for 50 °C in Qin *et al* (2014). In the case $T > 55$ °C, the overall frequency factor and activation energy become $A = 1.19 \times 10^{19}\ s^{-1}$ and $\Delta E = 125.5 \times 10^3\ J\ mol^{-1}$ respectively, which are within the values for 70 °C in Qin *et al* (2014).

Different intrinsic mechanisms can contribute to the slow death of a damaged cell, including apoptosis, necroptosis and autophagy. Models of apoptosis and the caspase mechanisms involve complex protein dynamics and would be suitable for the estimation of delayed thermal cell death (Pearce 2013). In this work, we follow a simpler approach similar to O'Neill *et al* (2011), which uses a threshold value for the cells in native state N, below which cell death is expected to occur. Since no data is available for cardiac myocytes, we consider the irreversible damage threshold to be $N \leqslant 0.8$ as in O'Neill *et al* (2011).

3. Results

3.1. Model calibration I: physiological response

The parameters in figure 1 have been first calibrated to provide physiological response for myocardial cells. In particular, the following conditions should be satisfied.

(1) No damage should be observed at body temperatures of 37 °C.

(2) No cell excitation occurs at temperatures higher than 43 °C (Zaltieri *et al* 2021).

(3) The damage is reversible for any ablation treatment time at temperatures up to 48 °C (Zaltieri *et al* 2021).

(4) Irreversible thermal damage occurs at temperatures between 50 °C and 56 °C after 60 s of thermal ablation (Haines 2011).

To test these cases, we simulated a commonly used experimental setup, in which the cells are placed in a thermal bath at a given temperature (Rylander *et al* 2005, O'Neill *et al* 2011). A constant temperature is applied to the tissue for a predefined period of time, followed by a thermal relaxation at body temperature of 37 °C.

Figure 2 shows the model response by applying three different temperatures for 60 s followed by a thermal relaxation period at a constant temperature of 37 °C. We allow the system to reach a stable state by using a final time of 25 min, in which the variations of the different states are below 5×10^{-6}. A 25 min exposure to a temperature at 37 °C (left panel) returns a variation in the level of native cells of about 1%, predicting no damage at all at body temperature. At temperatures of both 43 °C (central panel) and 48 °C (right panel), some initial

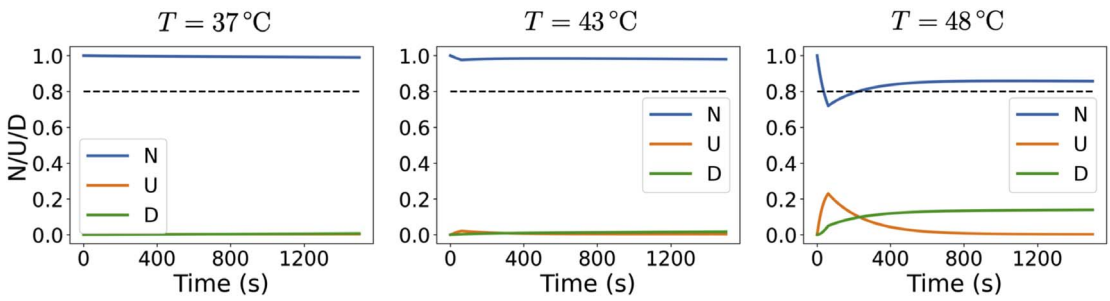

Figure 2. Response of the three-state tissue model to a 60 s exposure to a constant temperature (37 °C, 43 ° C, 48 °C) followed by a relaxation at body temperature (37 °C). The native state *N* lies above the 0.8 threshold after the relaxation and the inflicted damage is always reversible.

Table 1. Simulation protocol. RFA power: 20 W (standard protocols) or 90 W (HPSD). Saline: 17 ml min^{-1}. Ablation duration: 30 s (standard) or 4 s (HPSD). Relaxation duration: until the rate of change of the three states is below 5×10^{-6}.

Phase	Ablation	Post-ablation	Thermal relaxation
Power	On	Off	Off
Saline	On	Standby (2ml min^{-1})	Off
Duration	variable	30 s	Variable

damage is observed, but it always remains reversible as expected for myocytes. Note that we chose a duration of 60 s for temperature administration, which corresponds to typical cardiac ablation applications. In our numerical experiment we do not consider a temperature ramp, which is what is typically obtained from ablation studies (Toupin *et al* 2017, Zaltieri *et al* 2022), thus overestimating the exposure at the given temperatures. Despite this, the model still predicts a reversible damage as expected.

3.2. Model calibration II: lesion size assessment

For the second calibration step, we coupled the three-state model with our previously developed computational model for RFA, that is outlined in appendix B. For a comprehensive description of the model, we refer the reader to Petras *et al* (2019). The simulation protocol depends on the applied power and the flow rate of the cooling saline. It is organised in three phases as shown in table 1.

The duration of the ablation phase depends on the applied protocol (30 s for standard, 4 s for HPSD), while the thermal relaxation continues until the rate of change of the three states drops below 5×10^{-6}. Irreversible damage is assessed at the end of the thermal relaxation and it is identified by the threshold $N \leqslant 0.8$. The results are compared against the *in vitro* experimental results provided in Petras *et al* (2019) for two standard ablation protocols and against experimental data from Kotadia *et al* (2019) for high-power short-duration (HPSD) (see table 2).

For standard protocols we simulated virtual ablations of 20 W for 30 s on a porcine tissue, with applied forces of 10 g, 20 g, using a 6-pore open-irrigated catheter with spherical electrode tip (see Petras *et al* 2019 for the electrode specifications). The resulting lesion dimensions are in good agreement with the experimental data from Petras *et al* (2019), particularly for the depth. The lesion width *W* is consistently underestimated, but such shortcoming follows from a limitation of the RFA model in Petras *et al* (2019) which does not account for anisotropy in the electrical and thermal conductivities due to the cardiac fiber orientation.

For high-power short-duration (HPSD), we performed a virtual ablation of 90 W for 4 s on a simulated human ventricular tissue using a force of 10 g and a 6-pore open-irrigated catheter with a cylindrical tip (see the supplementary material of Petras *et al* (2021) for the electrode specifications). The resulting depth compares well with the experimental data from Kotadia *et al* (2019), however the lesion width is underestimated by the model, for the same reasons as before.

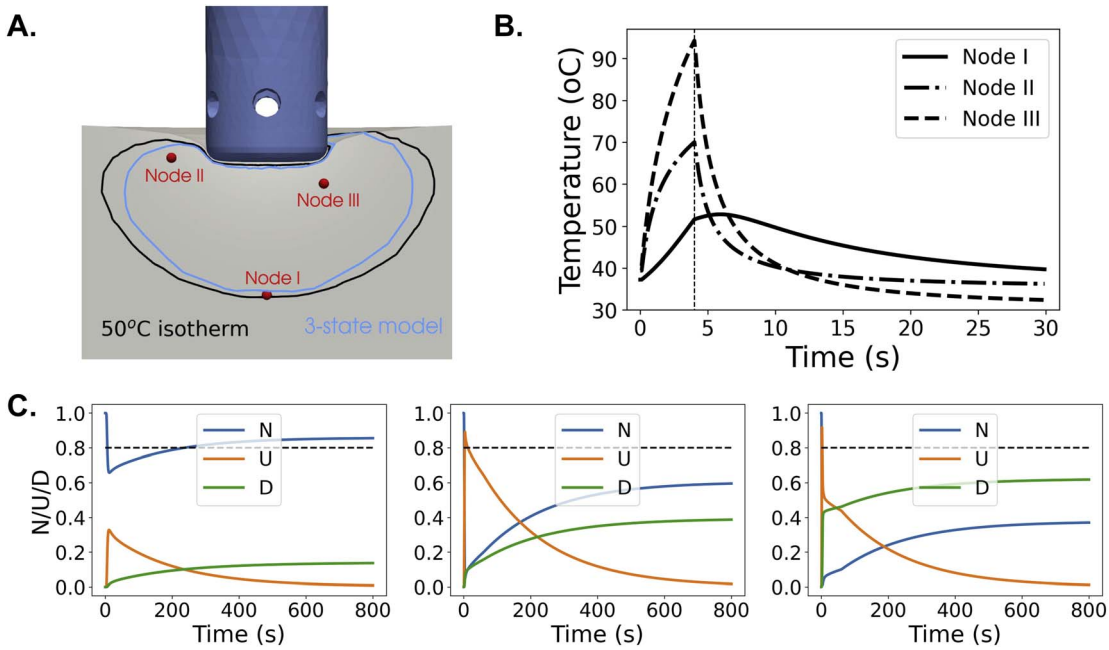

Figure 3. (A) Comparison of the resulting lesion of the HPSD protocol using the 50 °C isotherm at the end of the ablation and the three-state model after the relaxation time. (B) Temperature distribution of selected nodes during the ablation and the thermal relaxation. (C) The evolution of the three states for nodes I, II and III, ordered left-to-right.

Table 2. Comparison of lesion depth D and width W from the experimental data for standard (SP) (Petras *et al* 2019) and high-power short-duration (HPSD) protocols (Kotadia *et al* 2019) with the estimation provided by the three-state model. No contact force was reported for the experimental data with an *.

Protocol		Lesion dimension	Experimental data min–max	Three-state model
SP	(10 g, 20 W, 30 s)	D	1.4–3.1	2.15
		W	5.5–7.9	4.18
	(20 g, 20 W, 30 s)	D	2.2–4.6	3.36
		W	7.0–11.7	6.47
HPSD	(10 g, 90 W, 4 s)	D	2.6–3.6*	3.40
		W	5.9–10.3*	5.60

3.3. Thermal latency effect in HPSD ablations

Figure 3 takes a closer look at the results of the 90 W, 4 s, HPSD ablation protocol. As expected, the 50 °C isotherm predicts a larger irreversible thermal damage than the three-state model (panel A). Panel B presents the temporal evolution of the temperature in three different locations, whose positions are shown in panel A: one at the edge of the 50 °C isotherm (Node I), the other two closer to the electrode (Nodes II and III). A thermal latency effect is observed deep in the tissue, as shown by the temperature evolution for Node I (solid line): after the ablation stops, the temperature in Node I keeps increasing for a few seconds and remains above 50 °C before starting to drop. This effect may be suggesting that the lesion size is underestimated when the 50 °C isotherm is used. On the contrary, our simulations show that despite the thermal latency, the irreversible thermal damage is still smaller than the one predicted using the 50 °C isotherm. Panel C collects the solution in time of the three-state model for the three selected nodes, showing that the damage in Node I, that lies at the edge of the 50 °C isotherm, remains reversible, while Nodes II and III are irreversibly damaged.

3.4. Repeated HPSD ablations

Similarly to Petras *et al* (2021), we consider an ablation protocol with 2 subsequent HPSD applications of 90 W for 4 s with an in-between pause of 8 s, followed by 30 s of thermal relaxation. Using the model in Petras *et al* (2021) with a contact force of 5 g, the resulting evolution of the depth of the predicted damage is displayed in figure 4 using the 50 °C isotherm contour and the three-state model. The depth of the damaged area predicted by the isotherm becomes zero before the second application, which is a non-physiological result. In comparison,

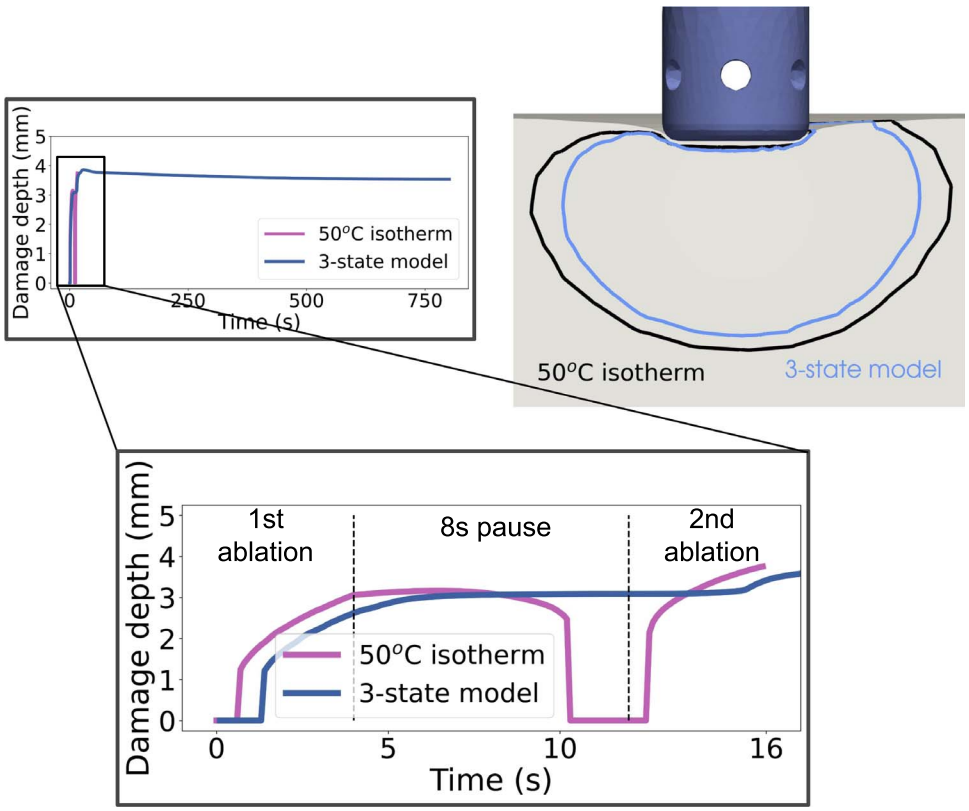

Figure 4. Repeated HPSD ablations. Evolution of the depth of the estimated damage area and the final predicted lesion size using the 50 °C isotherm and the three-state model.

the thermal damage depth predicted from the three-state model decelerates, however the pause between the ablations is too small to observe a shrinkage. The final lesion size after the two applications is once again overestimated by the 50 °C isotherm.

3.5. Ablation with catheter movement

We test the proposed method on the estimation of the irreversible damage region with a computational model that accounts for the catheter movement (as described in appendix B). Figure 5 summarizes the results for an ablation protocol of 30 W for 30 s, considering a heartbeat rate of 85 bpm. The temperature distribution is shown during the systolic and diastolic phases in panel A. To estimate the irreversible thermal damage, we consider either the 50 °C isotherm at the end of the ablation or the threshold $N \leqslant 0.8$ after the thermal relaxation time. The top left figure of panel B shows that the 50 °C isotherm, as usual, overestimates the lesion size. The bottom left figure of panel B shows the temperature evolution in time for two nodes, one near the surface (Node I) and one deeper in the tissue (Node II): temperature oscillations can be observed near the tissue surface during the cardiac cycle, due to the superficial cooling effect of the blood and the saline irrigation. This effect becomes negligible deeper in the tissue. A video showing this effect is available as supplementary material for this paper. The two figures on the right of panel B show the evolution of the predicted superficial tissue damage with the 50 °C and the three-state model. The temperature oscillations lead to severe oscillations in the surface damage predicted by the 50 °C isotherm, while the three-state model predicts a progressive increase of the damaged area. Thus, the similarity observed at the estimated final superficial lesions in the top left figure of panel B is merely coincidental, making the 50 °C isotherm an inaccurate and non-physiological estimation of the superficial tissue damage for dynamic ablation models.

4. Discussion

In this paper, we propose a modification of the three-state thermal cell death model in Park *et al* (2016) calibrated for cardiac myocytes. The model features an Arrhenius transition with variable absorption rate from native to unfolded states accounting for the reduction in the energy absorption as the temperature increases (Qin *et al* 2014). A similar approach has been reported in the literature for other types of cells (Dewey *et al* 1977, Pearce 2013).

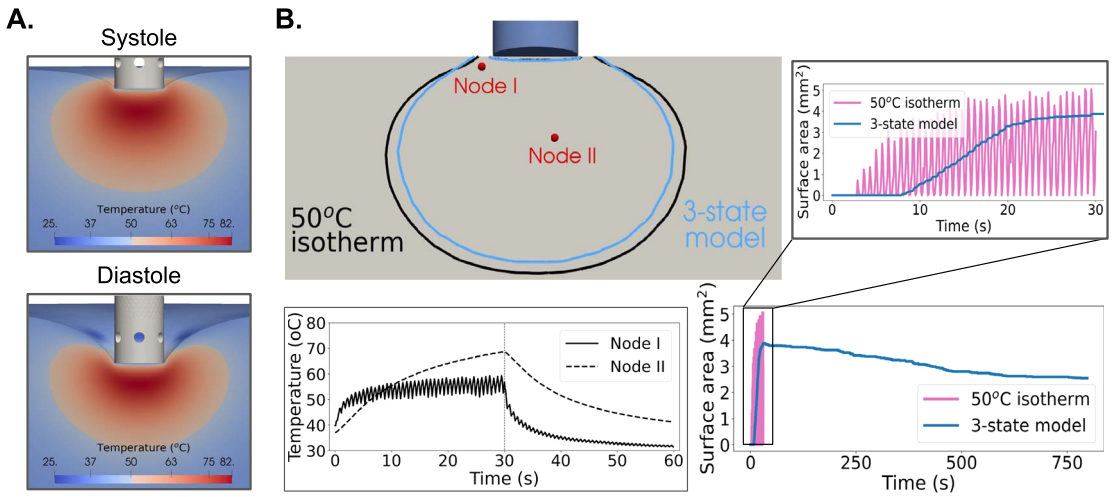

Figure 5. (A) The temperature distribution during the systolic (top) and diastolic (bottom) phases. (B) The irreversible thermal damage area given by the 50 °C isotherm after the ablation and the three-state model after the relaxation time at the undeformed configuration. The temperature evolution is displayed on two nodes, one close to the surface and one deeper in the tissue. The evolution of the superficial thermal damage area as estimated by the 50 °C isotherm and the three-state model.

The proposed method is capable of capturing the reversible damage that occurs due to intrinsic cellular protection mechanisms, which have been linked to the expression of heat shock proteins HSP70 (Rylander *et al* 2005). Irreversible damage due to direct protein denaturation is modeled by (1), while a threshold on the native state (following O'Neill *et al* 2011) captures the irreversible damage by other cellular mechanisms, such as apoptosis and necroptosis. Our work uses a threshold that is derived for human liver hepatocellular carcinoma (Hep G2) and human lung fibroblast (MRC-5) (O'Neill *et al* 2011), since no data is available for cardiac myocytes. Nonetheless, our results are in agreement with available data in the literature on cardiac cells (Haines 2011, Liu *et al* 2018, Zaltieri *et al* 2021).

The irreversible damage estimated by the proposed three-state model is capable of predicting lesions using the models in Petras *et al* (2019, 2021) that are in good agreement with the experimental data ranges (Kotadia *et al* 2019, Petras *et al* 2019). The limitations of the models in Petras *et al* (2019, 2021) due to the isotropic tissue biophysical properties are reflected in the predicted lesions by the proposed method.

The use of the long relaxation times until the rate of change of the three states is below 5×10^{-6} is reasonable considering the lengthy process of lesion evaluation after the ablation process in the experimental setups. This technique can also be used *in vivo*, since the irreversible damage area should be predicted after the tissue healing. However, other factors may affect the cellular viability *in vivo*, including the extent of the edema formation after the ablation (Yano *et al* 2020).

The three-state model is capable of capturing the inflicted damage on the tissue in cases of ablation models with catheter movement as well as models that use ablation protocols with multiple applications. For such models, the 50 °C isotherm may provide in some cases a crude estimation for the lesion size, however it can be very inaccurate and may lead to a serious overestimation of the irreversible damage area. The use of the three-state model allows for the introduction of alterations in the thermomechanical modelling of the tissue (Molinari *et al* 2022a) and its biophysical properties due to the inflicted thermal damage. These coupling aspects are part of our ongoing work.

Acknowledgments

This work has been partially supported by the State of Upper Austria. This research was funded in part by the Austrian Science Fund (FWF) P35374N. For the purpose of Open Access, the author has applied a CC BY public copyright licence to any Author Accepted Manuscript (AAM) version arising from this submission.

Data availability statement

All data that support the findings of this study are included within the article (and any supplementary information files). Data will be available from 23 February 2023.

Conflict of interest

The authors have no conflict of interest to declare.

Appendix A. Comparison with other lesion assessment methods

Table A1 collects a comparison with other commonly used lesion size assessment methods. The original three-state model (Park *et al* 2016) (calibrated for bovine chordae tendinae), with parameters $A_1 = 3.68 \times 10^{30}\ \mathrm{s}^{-1}$, $A_2 = 5.68 \times 10^{3}\ \mathrm{s}^{-1}$, $A_3 = 2.58 \times 10^{5}\ \mathrm{s}^{-1}$, $\Delta E_1 = 210 \times 10^{3}\ \mathrm{J\,mol}^{-1}$, $\Delta E_2 = 38.6 \times 10^{3}\ \mathrm{J\,mol}^{-1}$ and $\Delta E_3 = 47.2 \times 10^{3}\ \mathrm{J\,mol}^{-1}$ was used in Molinari *et al* (2022a, 2022b). The study in Molinari *et al* (2022a) uses a physiological threshold of $N_{\mathrm{thr}} = 0.8$, but lacks validation, as stated in the limitations therein: it is a proof of concept for thermomechanical remodelling during ablation and produces quite small lesions. Hence, it will not be used here. In Molinari *et al* (2022b), the threshold cutoff for irreversible thermal damage is raised to $N_{\mathrm{thr}} = 0.98$ in order to fit their modelling results to the available experimental data.

Another popular approach uses only two states, the native and the denaturated state. As described in Pérez *et al* (2022), the transition follows the Arrhenius model with $A = 7.39 \times 10^{39}\ \mathrm{s}^{-1}$ and $\Delta E = 257.7 \times 10^{3}\ \mathrm{J\,mol}$. The irreversible damage is identified using the $\Omega = 1$ isoline 90 s after the beginning of the ablation, corresponding to 63% dead cells, where

$$\Omega(t) = \int_0^t A e^{-\Delta E/(RT)} d\tau.$$

This isoline is the one used by Pérez *et al* (2022), despite the lack of physiological background behind this choice. In fact, $\Omega = 1$ was introduced to identify a trans-epidermal necrosis for skin burn (Henriques and Moritz 1947), but it has been used as a threshold for thermal injury to several other types of cells without any prior physiological assessment (Pearce 2013).

All models predict a lesion depth that lies within the experimental data for both SP and HPSD protocols. Note that in all cases a consistent underestimation of the width is observed due to the lack of anisotropy in the thermal and electrical conductivities of the RFA model (Petras *et al* 2019).

Table A1. Comparison of lesion depth D and width W from the experimental data for standard (SP) (Petras *et al* 2019) and high-power short-duration (HPSD) protocols (Kotadia *et al* 2019) with the estimation provided by four different lesion size assessment models. No contact force was reported for the experimental data with an *.

Protocol		Lesion dimension	Experimental data Min–max	Three-state model	50 °C-isotherm	Two-state model (Pérez *et al* 2022)	Three-state model (Molinari *et al* 2022b)
SP	(10 g, 20 W, 30 s)	D	1.4–3.1	2.15	2.58	1.66	1.53
		W	5.5–7.9	4.18	4.88	3.42	3.24
	(20 g, 20 W, 30 s)	D	2.2–4.6	3.36	3.69	3.01	2.90
		W	7.0–11.7	6.47	7.25	5.82	5.66
HPSD	(10 g, 90 W, 4 s)	D	2.6–3.6*	3.40	3.61	3.10	3.01
		W	5.9–10.3*	5.60	6.95	5.14	4.89

Appendix B. RFA computational model

B.1. Computational domain

The geometry of the model is similar to the one presented in Petras *et al* (2019): a box of $80 \times 80 \times 80\ \mathrm{mm}^3$ consisting of a board (Ω^{ext}) of $80 \times 80 \times 20\ \mathrm{mm}^3$ that models the external factors of the system, a tissue slab (Ω^{tissue}) of thickness H ($80 \times 80 \times H\ \mathrm{mm}^3$, where $H = 20$ mm for a simulated porcine tissue or $H = 12.5$ mm for a corresponding human ventricular slab), and a blood subdomain (Ω^{fluid}) of $80 \times 80 \times (60 - H)\ \mathrm{mm}^3$.

The domain includes an open catheter with a tip electrode ($\Omega^{\mathrm{electrode}}$) of length 3.5 mm and radius 7 Fr, featuring 6 irrigation pores of diameter 0.5 mm each (Petras *et al* 2022).

B.2. RFA model

By letting $\Omega = \Omega^{\text{tissue}} \cup \Omega^{\text{fluid}} \cup \Omega^{\text{electrode}} \cup \Omega^{\text{ext}}$, the equations of the model read as follows:

$$\begin{aligned} \nabla \cdot (\boldsymbol{\Sigma}(T)\nabla\Phi) &= 0, && \text{in } \Omega, \\ \rho c(T)\left(\frac{\partial T}{\partial t} + \mathbf{v}\cdot\nabla T\right) &= \nabla\cdot(\boldsymbol{K}(T)\nabla T) + \nabla\Phi\cdot\boldsymbol{\Sigma}(T)\nabla\Phi, && \text{in } \Omega, \\ \frac{\partial \mathbf{v}}{\partial t} + \mathbf{v}\cdot\nabla\mathbf{v} &= \nabla\cdot\mathbf{T}(\mathbf{v}, p), && \text{in } \Omega^{\text{fluid}}, \\ \nabla\cdot\mathbf{v} &= 0, && \text{in } \Omega^{\text{fluid}}, \end{aligned} \tag{3}$$

where ρ is the tissue density, $\boldsymbol{\Sigma}(\cdot)$ is the electrical conductivity tensor, Φ is the electrical potential, $c(\cdot)$ is the specific heat, T is the temperature, $\mathbf{v}$ is the velocity, $\boldsymbol{K}(\cdot)$ is the thermal conductivity tensor, p is the pressure scaled by the density and $\mathbf{T}(\mathbf{v}, p) = 2\mu\rho^{-1}(\nabla\mathbf{v} + \nabla\mathbf{v}^T)/2 - pI$ is the stress tensor of the Navier–Stokes equation, I is the identity tensor and μ is the dynamic viscosity of the blood. The irrigated saline is delivered to Ω^{fluid} through the inner electrode channels at a temperature of 28 °C (Squara *et al* 2014). A dispersive electrode is placed at the bottom of the domain, and a voltage drop is imposed on the interface between the electrode and the catheter shaft. For the remaining boundary conditions of the system we refer the reader to Petras *et al* (2019). Model (3) is solved with finite elements through a self-developed code implemented in FEniCSx (fenicsproject.org).

B.3. Catheter movement

The catheter movement is induced by the movement of the cardiac wall that, following the cardiac cycle, features a rapid contraction due to the ejection phase, followed by a slow relaxation and filling phase. Figure B1 shows the wall displacement, based on the left ventricular radial velocity data in Codreanu *et al* (2014) and using a reference of 85 heartbeats per minute corresponding to a normal heartbeat of a swine (Paslawska *et al* 2014). During the cardiac cycle, the cardiac wall is stiffening during the isovolumetric contraction (IVC) and remains stiff during the ejection phase (Couade *et al* 2009, Urban *et al* 2013).

The wall relaxation occurs during the diastole phase (Couade *et al* 2009, Urban *et al* 2013), in which it reaches the lowest elasticity value as shown in figure B1. Thus, in opposition to the wall movement, the catheter is located deeper in the tissue during the diastole and the indentation becomes shallow during the ejection phase. Using a contact force that ranges from 5 to 25 g, during the diastole and systole respectively, following values reported in the literature (Aizer *et al* 2018), the tip displacement is shown in figure B1.

The deformations of the cardiac tissue induced by the catheter tip movement are described by

$$\rho\frac{\partial^2\mathbf{u}}{\partial t^2} = \nabla\cdot\boldsymbol{\sigma}, \quad \text{in}\Omega^{\text{tissue}}, \tag{4}$$

where $\mathbf{u}$ is the displacement, $\boldsymbol{\sigma}$ is the stress tensor and Ω^{tissue} is the tissue subdomain, which is modelled as a nearly incompressible, hyperelastic, and orthotropic material (Usyk *et al* 2000). The relationship between $\boldsymbol{\sigma}$ and $\mathbf{u}$ is, as usual for hyperelastic materials

$$\boldsymbol{\sigma} = \frac{1}{J}\frac{\partial\Psi}{\partial F}F^T,$$

with F the deformation gradient, $J = \det F$ and the strain energy density

$$\Psi = \frac{c}{2}(e^Q - 1) + \frac{k}{2}\ln^2 J,$$

defined as the sum of two terms, the second of which penalises tissue compressibility via the weight k and the first of which models the deformation through the stiffness c and the anisotropy term

$$Q = \sum_{i,j} b_{i,j}E_{i,j}^2$$

with

$$E = \frac{F^TF - I}{2} \qquad \text{and} \qquad b = \begin{bmatrix} 5 & 10 & 2 \\ 10 & 6 & 2 \\ 2 & 2 & 3 \end{bmatrix}.$$

The fibers are considered parallel with the x-axis, and only the mechanical properties are considered anisotropic following the fiber distribution. The Fluid-Structure Interaction in our model is a one-way interaction, with the cardiac tissue moving freely as a consequence of the beating of the heart and the fluid domain following the imposed deformation. Algorithmically, we solve a time step of the tissue deformation, followed by a time step of the Navier–Stokes equations and finally a time step of the coupled potential and heat equations.

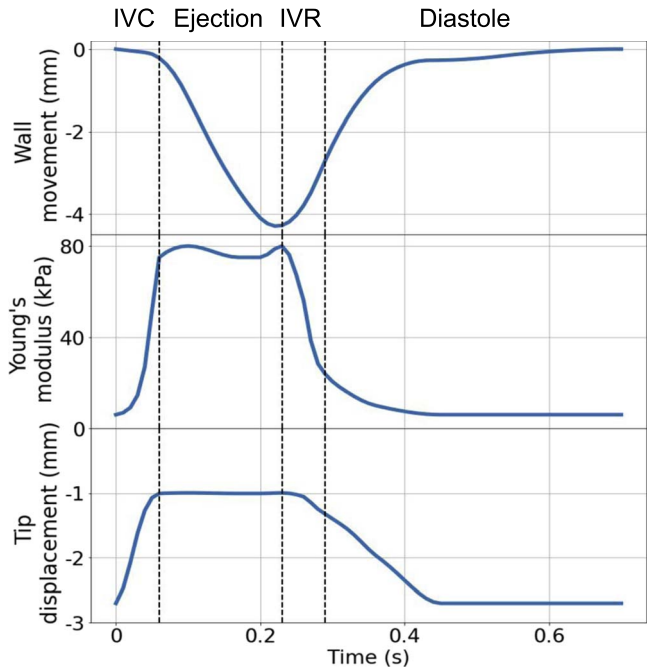

Figure B1. The wall movement, stiffening and the catheter tip displacement along the cardiac cycle.

We have a fixed contact surface, so we simply impose the displacement due to contact as a Dirichlet boundary condition. This is a reasonable approximation for a cylindrical tip electrode (Petras *et al* 2022).

Equation (4) is paired with system (3) and the coupled problem is defined, at time t, on the deformed geometry $\Omega \equiv \Omega_t$. In section 3.5 a porcine cardiac tissue is considered, and no blood inflow is imposed, due to the uncertainty in the blood flow velocity: the blood movement is thus driven by the wall movement during the cardiac cycle. In this experiment a cylindrical electrode is used to limit the computational complexity thanks to its fixed contact area with the tissue. The rest of the simulation protocol follows (Petras *et al* 2019). The coupled model (3)–(4) is solved with finite elements through a self-developed code implemented in FEniCSx (fenicsproject.org).

B.4. Parameters

The parameters of the models are based on Petras *et al* (2019) and Petras *et al* (2021) for standard and HPSD ablation protocols respectively. The thermal and electrical properties are isotropic and temperature dependent as detailed therein.

References

Ahn J W and Kim Y J 2021 Numerical analysis on the effects of saline injection and deformation for radiofrequency catheter ablation *Electronics (Switzerland)* **10** 1674

Aizer A *et al* 2018 Pacing mediated heart rate acceleration improves catheter stability and enhances markers for lesion delivery in human atria during atrial fibrillation ablation *JACC: Clin. Electrophysiol.* **4** 483–90

Codreanu I *et al* 2014 Normal values of regional and global myocardial wall motion in young and elderly individuals using navigator gated tissue phase mapping *Age* **36** 231–41

Couade M, Pernot M, Tanter M, Messas E, Bel A, Ba M, Hagege A-A and Fink M 2009 *Quantitative Imaging of Myocardium Elasticity Using Supersonic Shear Imaging* (Piscataway, NJ: IEEE) pp 151–4

Dewey W C, Hopwood L E, Sapareto S A and Gerweck L E 1977 Cellular responses to combinations of hyperthermia and radiation *Radiology* **123** 463–74

Gómez-Barea M, García-Sánchez T and Ivorra A 2022 A computational comparison of radiofrequency and pulsed field ablation in terms of lesion morphology in the cardiac chamber *Sci. Rep.* **12** 16144

González-Suárez A, Pérez J J, Irastorza R M, D'Avila A and Berjano E 2022 Computer modeling of radiofrequency cardiac ablation: 30 years of bioengineering research *Comput. Methods Programs Biomed.* **214** 106546

Gu K, Yan S and Wu X 2022 Effect of anisotropy in myocardial electrical conductivity on lesion characteristics during radiofrequency cardiac ablation: a numerical study *Int. J. Hyperth.* **39** 120–33

Haines D E 2011 Letter by Haines Regarding Article, 'Direct measurement of the lethal isotherm for radiofrequency ablation of myocardial tissue' *Circulation: Arrhythmia Electrophysiology* **4** e67

He L and Zhou B 2017 Cardiomyocyte proliferation: remove brakes and push accelerators *Cell Res.* **27** 959–60

Henriques F C Jr and Moritz A R 1947 Studies of thermal injury: I. The conduction of heat to and through skin and the temperatures attained therein. a theoretical and an experimental investigation *Am. J. Pathol.* **23** 530

Huang S K S and Wood M A 2014 *Catheter Ablation of Cardiac Arrhythmias* (Philadelphia, PA: Elsevier Health Sciences)
Kotadia I D, Williams S E and O'Neill M 2019 High-power, short-duration radiofrequency ablation for the treatment of AF *Arrhythmia Electrophysiol. Rev.* **8** 265
Liu F, Roy P, Shao Q, Jiang C, Choi J, Chung C, Mehra D and Bischof J C 2018 The role of protein loss and denaturation in determining outcomes of heating, cryotherapy, and irreversible electroporation on cardiomyocytes *J. Biomech. Eng.* **140** 061007
Molinari L, Gerardo-Giorda L and Gizzi A 2022a A transversely isotropic thermo-hyperelastic constitutive model of myocardial tissue with a three-state cell death dynamics for cardiac radiofrequency ablation *J. Mech. Phys. Solids* **161** 104810
Molinari L, Zaltieri M, Massaroni C, Filippi S, Gizzi A and Schena E 2022b Multiscale and multiphysics modeling of anisotropic cardiac RFCA: experimental-based model calibration via multi-point temperature measurements *Front. Physiol.* **13** 845896
O'Neill D P, Peng T, Stiegler P, Mayrhauser U, Koestenbauer S, Tscheliessnigg K and Payne S J 2011 A three-state mathematical model of hyperthermic cell death *Ann. Biomed. Eng.* **39** 570–9
Park C S, Hall S K, Liu C and Payne S J 2016 A model of tissue contraction during thermal ablation *Physiol. Meas.* **37** 1474–84
Paslawska U, Noszczyk-Nowak A, Paslawski R, Janiszewski A, Kiczak L, Zysko D, Nicpon J, Jankowska E A, Szuba A and Ponikowski P 2014 Normal electrocardiographic and echocardiographic (m-mode and two dimensional) values in polish landrace pigs *Plastic Reconstr. Surg.—Glob. Open* **56** 54
Pearce J A 2013 Comparative analysis of mathematical models of cell death and thermal damage processes *Int. J. Hyperth.* **29** 262–80
Pérez J J, D'Angelo R, González-Suárez A, Nakagawa H, Berjano E and d'Avila A 2022 Low-energy (360 j) radiofrequency catheter ablation using moderate power-short duration: proof of concept based on in silico modeling *J. Interventional Cardiac Electrophysiol* (https://doi.org/10.1007/s10840-022-01292-z)
Petras A, Leoni M, Guerra J M, Jansson J and Gerardo-Giorda L 2019 A computational model of open-irrigated radiofrequency catheter ablation accounting for mechanical properties of the cardiac tissue *Int. J. Numer. Methods Biomed. Eng.* **35** e3232
Petras A, Weidmann Z M, Ferrero M E, Leoni M, Guerra J M and Gerardo-Giorda L 2022 Impact of electrode tip shape on catheter performance in cardiac radiofrequency ablation *Heart Rhythm O2* **3** 699–705
Petras A, Weidmann Z M, Leoni M, Gerardo-Giorda L and Guerra J M 2021 Systematic characterization of high-power short-duration ablation: insight from an advanced virtual model *Front. Med. Technol.* **3** 747609
Qadri A M, Chia N J Y and Ooi E H 2017 Effects of saline volume on lesion formation during saline-infused radiofrequency ablation *Appl. Math. Modell.* **43** 360–71
Qin Z, Balasubramanian S K, Wolkers W F, Pearce J A and Bischof J C 2014 Correlated parameter fit of Arrhenius model for thermal denaturation of proteins and cells *Ann. Biomed. Eng.* **42** 2392–404
Rylander M N, Diller K R, Wang S and Aggarwal S J 2005 Correlation of hsp70 expression and cell viability following thermal stimulation of bovine aortic endothelial cells *J. Biomech. Eng.* **127** 751–7
Singh S and Melnik R 2019 Coupled thermo-electro-mechanical models for thermal ablation of biological tissues and heat relaxation time effects *Phys. Med. Biol.* **64** 245008
Singh S and Melnik R 2020 Thermal ablation of biological tissues in disease treatment: a review of computational models and future directions *Electromagn. Biol. Med.* **39** 49–88
Squara F, Maeda S, Aldhoon B, Marginiere J, Santangeli P, Chik W W, Michele J, Zado E and Marchlinski F E 2014 In vitro evaluation of ice-cold saline irrigation during catheter radiofrequency ablation *J. Cardiovasc. Electrophysiol.* **25** 1125–32
Toupin S *et al* 2017 Feasibility of real-time mr thermal dose mapping for predicting radiofrequency ablation outcome in the myocardium *in vivo J. Cardiovasc. Magn. Reson.* **19** 14
Urban M W, Pislaru C, Nenadic I Z, Kinnick R R and Greenleaf J F 2013 Measurement of viscoelastic properties of *in vivo* swine myocardium using lamb wave dispersion ultrasound vibrometry (lduv) *IEEE Trans. Med. Imaging* **32** 247–61
Usyk T P, Mazhari R and McCulloch A D 2000 Effect of laminar orthotropic myofiber architecture on regional stress and strain in the canine left ventricle *J. Elast.* **61** 143–64
Yano M *et al* 2020 Comparison of myocardial injury and inflammation after pulmonary vein isolation for paroxysmal atrial fibrillation between radiofrequency catheter ablation and cryoballoon ablation *J. Cardiovasc. Electrophysiol.* **31** 1315–22
Zaltieri M, Massaroni C, Cauti F M and Schena E 2021 Techniques for temperature monitoring of myocardial tissue undergoing radiofrequency ablation treatments: an overview *Sensors* **21** 1453
Zaltieri M, Rossi P, Bianchi S, Polselli M, Niscola M, Fanti V, Massaroni C, Schena E and Cauti F M 2022 Spatial temperature reconstructions in myocardial tissues undergoing radiofrequency ablations by performing high-resolved temperature measurements *J. Interventional Cardiac Electrophysiol.* **64** 173–182